Monthly Notices of the ROYAL ASTRONOMICAL SOCIETY
MNRAS **540,** 175–189 (2025) https://doi.org/10.1093/mnras/staf743
Advance Access publication 2025 May 09

Formation of large circumstellar discs in multiscale, ideal-MHD simulations of magnetically critical, massive pre-stellar cores

Chong-Chong He ★ and Massimo Ricotti ★
Department of Astronomy, University of Maryland, College Park, MD 20742, USA

Accepted 2025 April 28. Received 2025 March 21; in original form 2023 April 11

ABSTRACT

The formation of circumstellar discs is a critical step in the formation of stars and planets. Magnetic fields can strongly affect the evolution of angular momentum during prestellar core collapse, potentially leading to the failure of protostellar disc formation. This phenomenon, known as the magnetic braking catastrophe, has been observed in ideal-magentohydrodynamics (MHD) simulations. In this work, we present results from ideal-MHD simulations of circumstellar disc formation from realistic initial conditions of strongly magnetized, massive cores with masses between 30 and 300 $M_\odot$ resolved by zooming into giant molecular clouds (GMCs) with masses $\sim 10^4$ $M_\odot$ and initial mass-to-flux ratios $0.6 \leq \mu_0 \leq 3$. Due to the large turbulence in the gas, the dominant vertical support of discs is turbulent motion, while magnetic and turbulent pressures contribute equally in the outer toroid. We find that large Keplerian discs can form even in magnetically critical or near-critical cores due to the suppression of magnetic braking by highly turbulent and incoherent magnetic field topologies. Only cores in GMCs with $\mu_0 < 1$ fail to form discs. Instead, they collapse into a sheet-like structure and produce numerous low-mass stars. We also discuss a universal B–ρ relation valid over a large range of scales from the GMC to massive cores, irrespective of the GMC magnetization. This study differs from the vast literature on this topic which typically focus on smaller mass discs with idealized initial and boundary conditions, therefore providing insights into the initial conditions of massive prestellar core collapse and disc formation.

Key words: MHD – stars: formation – stars: massive – stars: protostars – ISM: magnetic fields.

1 INTRODUCTION

The formation of protostellar discs is ubiquitous during the collapse of prestellar cores. As a molecular core collapses under its own self-gravity, the angular momentum of the gas will slow down its collapse at small scales promoting the formation of a protostellar disc. This simple argument of conservation of angular momentum is corroborated by observations, also suggesting that protostellar disc formation is a natural byproduct of the star formation process (O'dell & Wen 1992; Tobin et al. 2012; Murillo et al. 2013; Codella et al. 2014; Lee et al. 2017).

However, molecular clouds are observed to be permeated by magnetic fields (Crutcher 1999; Lee et al. 2017), which can in principle strongly affect the evolution of angular momentum during the core collapse. The twisting of the magnetic field lines produced by the disc rotation in the flux-freezing regime of ideal magnetohydrodynamics (MHD), can apply a force counter to the rotation velocity, also known as magnetic braking, effectively slowing down rotation and increasing radial gas infall. In idealized numerical MHD simulations, the time-scale of the braking can become so short that protostellar discs fail to form or are much smaller than the observed sizes, a phenomenon known as 'the magnetic braking catastrophe' (e.g. Allen, Li & Shu 2003; Galli et al. 2006; Hennebelle & Fromang 2008; Li et al. 2014). Indeed, disc formation should be completely suppressed in the strict ideal MHD limit for the level of core magnetization deduced from observation – the angular momentum of the idealized collapsing core is nearly completely removed by magnetic braking close to the central object (e.g. Mestel & Spitzer 1956; Mellon & Li 2008). These results seem to be in contrast to the observed existence of Keplerian discs around protostellar objects. While some simulations with ideal MHD have successfully reproduced the observed sizes of certain large Class 0 and Class I protostellar discs (~ 100 au) as revealed by recent radio/mm and optical/IR observations (Zapata et al. 2007), these simulations often fail to account for the extremely large discs ($\gtrsim 1000$ au) that have been observed recently (Johnston et al. 2020).

Magnetic fields support charged gas against gravitational collapse. A common characterization of the relative importance of the gravitational and magnetic forces in a molecular cloud or core is the normalized mass-to-flux ratio,

$$\mu \equiv \frac{M/\Phi_B}{M_\Phi/\Phi_B} = \frac{M}{M_\Phi}, \tag{1}$$

where M is the total mass contained within a spherical region of radius R, $\Phi_B = \pi R^2 B$ is the magnetic flux threading the surface of the sphere assuming a uniform magnetic field strength B, and

$$M_\Phi = c_\Phi \frac{\Phi_B}{\sqrt{G}}, \tag{2}$$

★ E-mail: chongchong.he@anu.edu.au (CCH); ricotti@umd.edu (MR)

is the magnetic critical mass, the mass at which the magnetic and gravitational forces balance each other. The constant c_Φ is a dimensionless coefficient that depends on the assumed geometry of the system. For a spherical cloud of uniform density, $c_\Phi = \sqrt{10}/(6\pi) = 0.168$. For a more centrally concentrated geometry, e.g. a non-singular isothermal sphere, the equivalent geometrical factor c_Φ is up to 70 per cent higher and μ is 40 per cent lower than the uniform density case (see Appendix A).

An alternative definition of the mass-to-flux ratio is

$$\mu \equiv \sqrt{\frac{|W|}{\mathcal{B}}}, \tag{3}$$

where W represents the gravitational potential energy and $\mathcal{B}$ denotes the magnetic energy. Equation (3) is equivalent to equation (1), and by equating the two definitions, the value of c_Φ can be determined.

In a sub-critical cloud (defined as a cloud with $\mu < 1$), the magnetic field should prevent the collapse of the cloud core altogether. Observations suggest typical values of $\mu \approx 2$–10 in molecular cloud cores (e.g. Crutcher 1999; Bourke et al. 2001), and this value could be even smaller after correcting for projection effects (Li et al. 2013a). Moreover, analytical predictions (Joos, Hennebelle & Ciardi 2012) suggest that there are no centrifugally supported discs in models with $\mu \leq 10$; what appear instead are pseudo-discs, which are disc-shape overdensities that are not rotationally supported (Galli & Shu 1993).

Simulating the formation and evolution of individual stars requires resolving the 'opacity limit' for fragmentation – the critical density above which the gas becomes optically thick to cooling radiation, leading to gas heating and a halt to fragmentation (Rees 1976). This critical density is 10^{10}–10^{11} cm^{-3} at solar metallicities. There is a vast literature studying collapsing gas near this density regime using both ideal MHD simulations (Hennebelle & Ciardi 2009; Joos et al. 2012, 2013; Santos-Lima, de Gouveia Dal Pino & Lazarian 2012; Li, Krasnopolsky & Shang 2013b; Seifried et al. 2013; Li et al. 2014; Fielding et al. 2015; Gray, McKee & Klein 2018; Lewis & Bate 2018; Tsukamoto et al. 2018; Lam et al. 2019; Hirano et al. 2020; Wurster & Lewis 2020), or non-ideal MHD studies/simulations (Machida, Inutsuka & Matsumoto 2011; Masson et al. 2016; Wurster, Price & Bate 2016; Kölligan & Kuiper 2018; Zhao et al. 2018; Lam et al. 2019; Wurster & Bate 2019; Kuffmeier, Zhao & Caselli 2020; Tsukamoto et al. 2020; Mignon-Risse et al. 2021; Commerçon et al. 2022; Mignon-Risse et al. 2023). We refer to Tsukamoto et al. (2023) for a comprehensive review on this topic. Each of these previous studies, in addition to facing specific constraints due to computational cost/limitations, focus on different physics questions and has initial conditions that typically apply to describing traditional cores/circumstellar discs around solar-type stars. Typically, the mass of the molecular clouds studied does not exceed 500 M$_\odot$, with the most common limit of around 100 M$_\odot$. Moreover, most of these simulations usually assume idealized initial and boundary conditions for the discs, along with artificially introduced turbulence, which may not fully capture the complexities of the star formation processes in a realistic molecular cloud environment.

The main incremental improvement of this work, when compared to existing literature, is the adoption of realistic initial and boundary conditions for the collapse of high-mass prestellar cores. Here, we stress two points: (i) the masses of the cores presented in this study of circumstellar disc formation are significantly larger than in most previous studies: between 30 and 300 M$_\odot$; (ii) We simulate these core adopting realistic initial conditions by zooming into strongly magnetized cores within a coarser resolution simulations of an $\sim 10^4$ M$_\odot$ giant molecular clouds (GMCs), along with realistic boundary conditions from the co-evolving GMC. This paper is an extension of the work presented in He & Ricotti (2023; hereafter, Paper I), in which we studied the formation and fragmentation of high-mass prestellar cores and the formation of large circumstellar discs. In this work, we focus on the magnetic phenomenon and the effects of varying the cloud magnetization, in the ideal-MHD regime. In Section 4, we discuss how our results compare to the extensive body of literature on ideal- and non-ideal MHD simulations of circumstellar discs.

The rest of this article is organized as follows. We describe the methods in our simulations in Section 2. We present the results in Section 3, including an analysis of why the magnetic braking catastrophe does not prevent disc formation. A discussion in light of previous literature is presented in Section 4, and a summary and conclusions in Section 5.

2 METHOD

In Paper I we have conducted a set of 'zoom-in' radiation-MHD simulations of prestellar core formation and evolution within collapsing GMCs. In this work, we extend the set of simulations to explore the effects of stronger magnetic fields. We present a suite of six 'zoom-in' simulations of prestellar cores in molecular clouds with varying magnetization and turbulence. We summarize the key parameters of the simulated GMCs and cores in Table 1. Two GMCs, μ`3Ma15` and μ`3Ma7` are fiducial runs with the same initial magnetization ($\mu_0 = 3.0$) as those presented in Paper I and in He, Ricotti & Geen (2019), in which we present the results for the larger scale GMCs evolution. The two clouds have initial turbulent Mach numbers $\mathcal{M} = 15$ and $\mathcal{M} = 7$ and masses of 3×10^4 and 3×10^3 M$_\odot$, respectively. These two GMCs are the XS-C and M-C clouds in He et al. (2019), respectively. They represent clouds with mass, density, and magnetization similar to Milky Way GMCs. They both have an initial average number density of 200 cm^{-3}. The other four GMCs on which we zoom in (μ`1Ma15`, μ`1Ma7`, μ`0.6Ma15`, and μ`0.6Ma7`) have the same properties as the two fiducial clouds but increased magnetic field intensities with $\mu_0 = 1.0$ and $\mu_0 = 0.6$, as shown by the name of the run. We also list the Alfven Mach number $\mathcal{M}_A = v/v_A$, where v is the plasma velocity and v_A is the Alfven speed, and the Plasma beta $\beta = P_{\rm th}/P_{\rm mag}$, which is the ratio of thermal pressure to magnetic pressure, of the initial GMC, as well as the spatial resolution $\Delta x_{\rm min}$ of the zoom-in simulations.

For all the six zoom-in simulations mentioned above, we zoom into the first cores forming in each GMC and study their subsequent collapse. In this work, we also include two extra cores selected from Paper I: (1) μ`3Ma7-hires`, which corresponds to Core *A-hr* in Paper I, is a higher resolution zoom-in version of μ`3Ma7`; (2) μ`3Ma15-large` corresponds to Core *B* in Paper I, which is a very massive core that forms in the later stage of star formation in the fiducial GMC μ`3Ma15`.

The sink particle (star formation) and stellar feedback recipes and the 'zoom-in' method used in this work are described in Paper I. Here, we provide only a brief summary. We perform simulations of star formation using the grid-based adaptive mesh refinement (AMR) MHD code RAMSES (Teyssier 2002; Fromang, Hennebelle & Teyssier 2006; Bleuler & Teyssier 2014). Radiation transfer is modelled using a moment-based method with the M1 closure relationship for the Eddington tensor (RAMSES-RT; Rosdahl et al. 2013). The ionizing photons emitted from stars interact with neutral gas and we keep track of the time-dependent ionization chemistry of atomic hydrogen and helium, but we do not include the chemical evolution of the molecular phase and metal chemistry, used only for cooling/heating rates, is treated assuming equilibrium abundances. Heating from

Table 1. List of zoom-in simulations presented in this paper. Col. (2): core mass based on gas above a density threshold of 3000 cm^{-3}. Col. (3): core mass based on gas within a radius of 0.1 pc from the density peak. All the cores are chosen as the first star-forming core in the corresponding GMC, except for the one with a *, which is chosen from the later stage of the GMC evolution and it is a very massive core with over 100 $M_\odot$.

GMC/core name	$m_{3000}(M_\odot)$	$m_{0.1pc}$ $(M_\odot)$	μ_0	$\mathcal{M}$	B (μG)	$\mathcal{M}_A$	β	Δx_{min} (au)	n_{sink} (cm^{-3})
μ3Ma15	30	12	3	15	10	5	0.1	60	8×10^8
μ3Ma15-large*	130	30	3	15	10	5	0.1	60	8×10^8
μ1Ma15	40	30	1	15	30	1.7	0.01	60	8×10^8
μ0.6Ma15	300	25	0.6	15	50	1	0.004	60	8×10^8
μ3Ma7	27	10	3	7	5	5	0.5	29	4×10^9
μ3Ma7-hires	27	10	3	7	5	5	0.5	7	6×10^{10}
μ1Ma7	100	15	1	7	15	1.7	0.06	29	4×10^9
μ0.6Ma7	60	10	0.6	7	25	1	0.02	29	4×10^9

photoionization and cooling from hydrogen and helium, metals, and dust grains are implemented. Cooling below 10 K is shut down to keep the temperature floor at 10 K. The photoionization feedback from stars heats the gas, dispersing the cloud and quenching star formation.

The baseline simulations of GMCs are started from a spherically symmetric structure with density profile of a non-singular isothermal sphere in hydrostatic equilibrium with a surrounding low-density shell, in which gravity is nearly balanced by turbulent motions ($\alpha \equiv K/|W| = 0.4$). The clouds measure 3×10^3 $M_\odot$ (3×10^4 $M_\odot$) in mass and 4.6 pc (10 pc) in radius for the `Ma7` (`Ma15`) runs. The simulation box is 4 times larger than the diameter of the cloud to follow the expansion and dissolution of the cloud. In the initial condition, the density profile is perturbed with a turbulent velocity field, analogously to the set up used in Geen, Soler & Hennebelle (2017). The turbulence of the clouds follows a Kolmogorov power spectrum with random phases and has an amplitude such that the cloud is approximately in virial equilibrium. The magnetic field is parallel to the x-axis, and its strength at the $y - z$ plane crossing the cloud center decreases with distance to cloud centre so that the Alfven speed is kept constant. The field strength at the cloud center is listed at the 6th column of Table 1. We let the cloud relax for three free-fall times to allow the turbulence to develop before turning on full gravity and sink particle formation (i.e. star formation). Adaptive mesh refinement is applied to the whole domain to make sure at any time and any location the local Jeans length, $L_J = c_s\sqrt{\pi/(G\rho)}$, is resolved by at least 10 grid points. The maximum refinement level l_{max} is set to 14 in the whole domain.

In the zoom-in simulations presented in this work, we rerun each GMC simulation starting right before the first sink particle (prestellar core) forms in the baseline run. We, therefore, define a 'core' in our simulations as the progenitor of a sink particle or binary sink particles in the baseline simulation. In physical terms, 'cores' are the largest isothermal spheres that form inside a GMC and are in hydrostatic equilibrium (see Paper I for evidence that the density profile of these cores resembles that of a Bonnor–Ebert sphere). We define a 'zoom' region, about 2 pc in size, at the location where the first core forms and set a higher refinement level of $l_{max} = 18$ inside this region. We measure the core mass (Table 1) using two methods: (1) by applying a density threshold of 3000 cm^{-3}, and (2) by considering the mass of gas encompassed with a 0.1 pc radius. This approach is motivated by the fact that, during the isothermal phase, each core has a $\propto r^{-2}$ density profile that extends up to a few $\times 10^5$ au; within this range, the mass enclosed is directly proportional to the radius enclosed. To reach the best possible resolution with manageable computational power, we use a nested refinement structure where l_{max} increases as it gets closer to the domain centre. The critical density for sink formation is $n_{sink} = 3.6 \times 10^9$ and 7.7×10^8 cm^{-3} for the `Ma7` and `Ma15` clouds, respectively, guided by the criterion that a Jeans length at $c_s = 0.24$ km s^{-1}, the sound speed of cold neutral medium at ~ 10 K, must be resolved by no less than 5 grids. We stop the zoom-in simulations when either the disc structure disappears (in case where discs do form) or when the core is dispersed by stellar feedback and we are convinced that no large discs will form.

2.1 Disc definition

In order to identify discs and study their properties in the zoom-in simulations, we work in a cylindrical frame of reference centred on the disc with $z-$axis parallel to the angular momentum of the overdense gas inside the core. In all our discussions of the disc property, the density, velocity, pressure, and magnetic field are an azimuthal average weighted by mass.

We define a disc using two principal criteria: a density threshold and rotational support. The density threshold is set at 10^6 cm^{-3}, a value limited by resolution but sufficiently high to avoid large spiral arms. This threshold, roughly consistent with the literature (Joos et al. 2012, 2013), helps in distinguishing potential disc structures, which can manifest either as a flat, pancake-like shape, or a radiant shape with a thinner inner disc and thick outer part (as illustrated in Fig. 2). For a structure to be classified as a disc, it also must exhibit disc-like geometry and be rotationally supported. We define 'rotational support' empirically, quantifying it with the Keplerianity parameter, which is the ratio of azimuthal velocity to the Keplerian velocity, $\beta_K \equiv v_\phi/v_{kep}$. We define the Keplerian velocity as the velocity of a test particle orbiting around a central mass of M_{encl} in spherical orbit, $v_{kep} \equiv \sqrt{GM_{encl}/R}$, where M_{encl} denotes the total mass enclosed within radius R, which includes both gas and sink particles. We impose two criteria for β_K. The first criterion is $\beta_K \geq 0.5$, which corresponds to a rotational-to-gravitational energy ratio $K_r/|W| = 0.5\beta_K^2 \geq 0.125$. The second criterion is that the disc is truncated at the radius where β_K begins to decline, thereby excluding the less-dense, puffy envelope. In summary, we define the disc radius as the minimum between the radius defined by the density threshold and by the rotational support criteria.

For visualization and further analysis (see Section 3), we generate a contour plot representation of the disc in surface density plots (for instance see white contours in Figs 2 and 3). The white lines representing the face-on discs are iso-contours of the surface density with thresholds chosen such that the average radius of

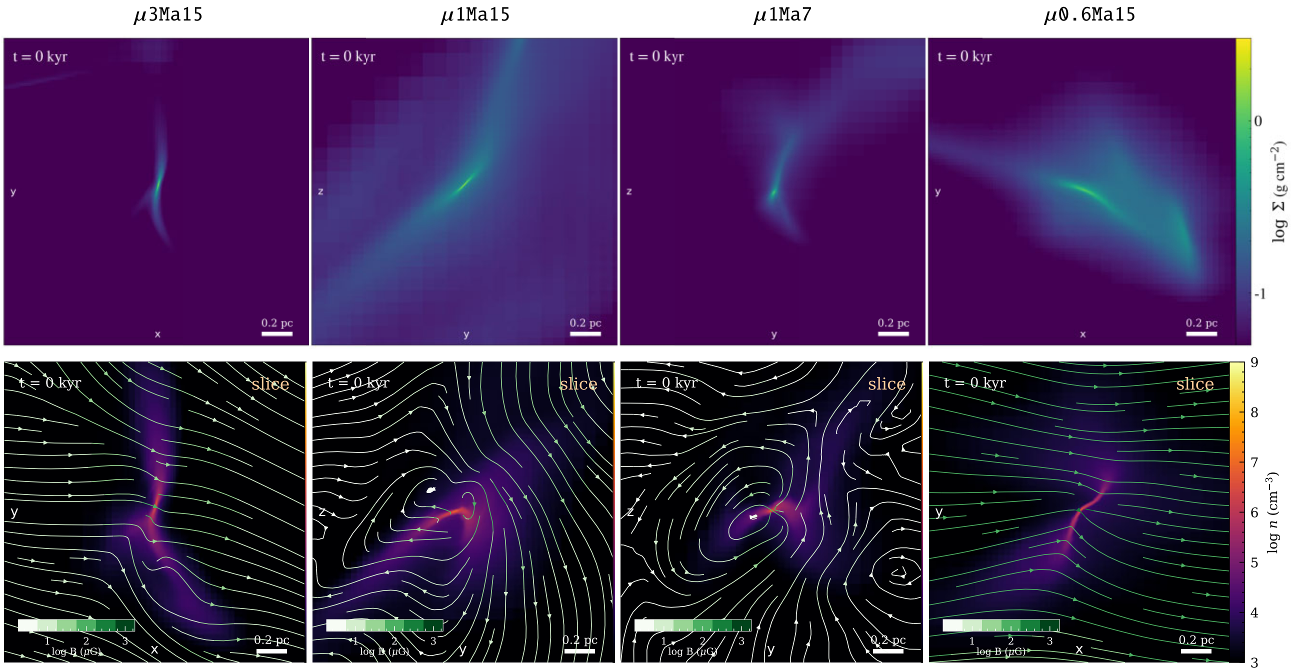

Figure 1. (*Top*) Surface density of the cores μ`3Ma15`, μ`1Ma15`, μ`1Ma7`, and μ`0.6Ma15`, showing their morphology at $t = 0$, shortly before the formation of stars. (*Bottom*) Density slices of the corresponding cores centred at the peak density overplotted with magnetic field streamlines. The field of view and viewing angle orientation are the same as in the top panels. The magnetic field streamlines are colour coded according to their magnitudes and a colourbar is shown at the bottom-left corner. Note how the surface density of the core μ`0.6Ma15` does not intuitively reflect the actual geometry of its sheet-like shape.

the contour is roughly the same as the disc radius as defined above.

2.2 Calculation of radial profiles

In the subsequent discussion of disc properties, we present the radial profiles of parameters such as the Alfven velocity in two coordinate systems.

During the core phase, we use spherical coordinates and express the profiles as a function of the spherical radius $r_{\rm sph}$, which represents the distance from the core centre. These quantities are averaged over a thin shell at radius $r_{\rm sph}$.

For the disc phase, we use cylindrical coordinates, and express the profiles as a function of the cylindrical radius $r_{\rm cyl}$. The radial profile of a quantity q (e.g. the Alfven velocity v_A, azimuthal velocity v_ϕ, and sound speed c_s) is calculated as the density-weighted average over a cylindrical shell:

$$q(r_{\rm cyl}) = \frac{\int_{r_{\rm cyl}-\Delta r_{\rm cyl}}^{r_{\rm cyl}+\Delta r_{\rm cyl}} \int_0^{2\pi} \int_{-z_0}^{z_0} q(\mathbf{r})\rho r\,{\rm d}r\,{\rm d}\phi\,{\rm d}z}{\int_{r_{\rm cyl}-\Delta r_{\rm cyl}}^{r_{\rm cyl}+\Delta r_{\rm cyl}} \int_0^{2\pi} \int_{-z_0}^{z_0} \rho r\,{\rm d}r\,{\rm d}\phi\,{\rm d}z}, \quad (4)$$

where $\Delta r_{\rm cyl}$ denotes the thickness of the cylindrical shell, typically equivalent to the size of a few grid cells, and $z_0 = 100$ au is the height of the cylinder, roughly corresponding to disc thickness in our simulation. The calculation of the z-component turbulent velocity, $\sigma(v_z)$, involves additional steps. First, we calculate the cylindrically averaged z-component velocity, $\bar{v}_z(r_{\rm cyl})$, using equation (4) with $q(\boldsymbol{r}) = v_z(\boldsymbol{r})$. Next, we compute the variance by applying equation (4) with $q(\boldsymbol{r}) = (v_z(\boldsymbol{r}) - \bar{v}_z(r_{\rm cyl}))^2$. Finally, $\sigma(v_z)$ is the square root of the variance. The radial profiles of the radial and azimuthal components of the magnetic field, B_r and B_ϕ, are obtained in a similar way. However, in this case, $q = B^2$ is used without applying a density weight to account for the volume-integrated magnetic energy density, and the final result is taken a square root to obtain the cylindrically averaged quantities.

3 RESULTS

The key result from our suite of simulations is that large, Keplerian discs form at the centres of magnetically (near-)critical cores. We present the disc properties and statistics of the stars/sink particles in Table 2. Between 2 and 20 stars emerge from the collapse of a massive core, with a large, rotationally supported disc structure forming around the central massive star or binary, while additional stars are distributed throughout or at the vicinity of the disc. We refer to our companion paper of this series (Paper I) for more details on the sink mass functions and a detailed study on disc properties. In this paper, we focus on the role of the large-scale magnetic field in the GMC in determining the formation of these large discs and their properties. Below we present results for a set of simulations with different μ and turbulent Mach number, focusing on the cores morphologies and evolution (Section 3.1), the magnetic field–gas density relationship (Section 3.2), the vertical support of the discs (Section 3.2), and a critical analysis of the magnetic braking problem (Section 3.4).

3.1 Morphology of gas density and magnetic field in cores

For the same GMC simulation and sink particle we zoom into, the strength of the background magnetic field has an effect on the early phase of collapse and the initial morphologies of the collapsing cores. The top row of Fig. 1 shows the surface density of the gas for a representative set of 4 simulations while the bottom row shows the density in a slice through the same filament and the magnetic field

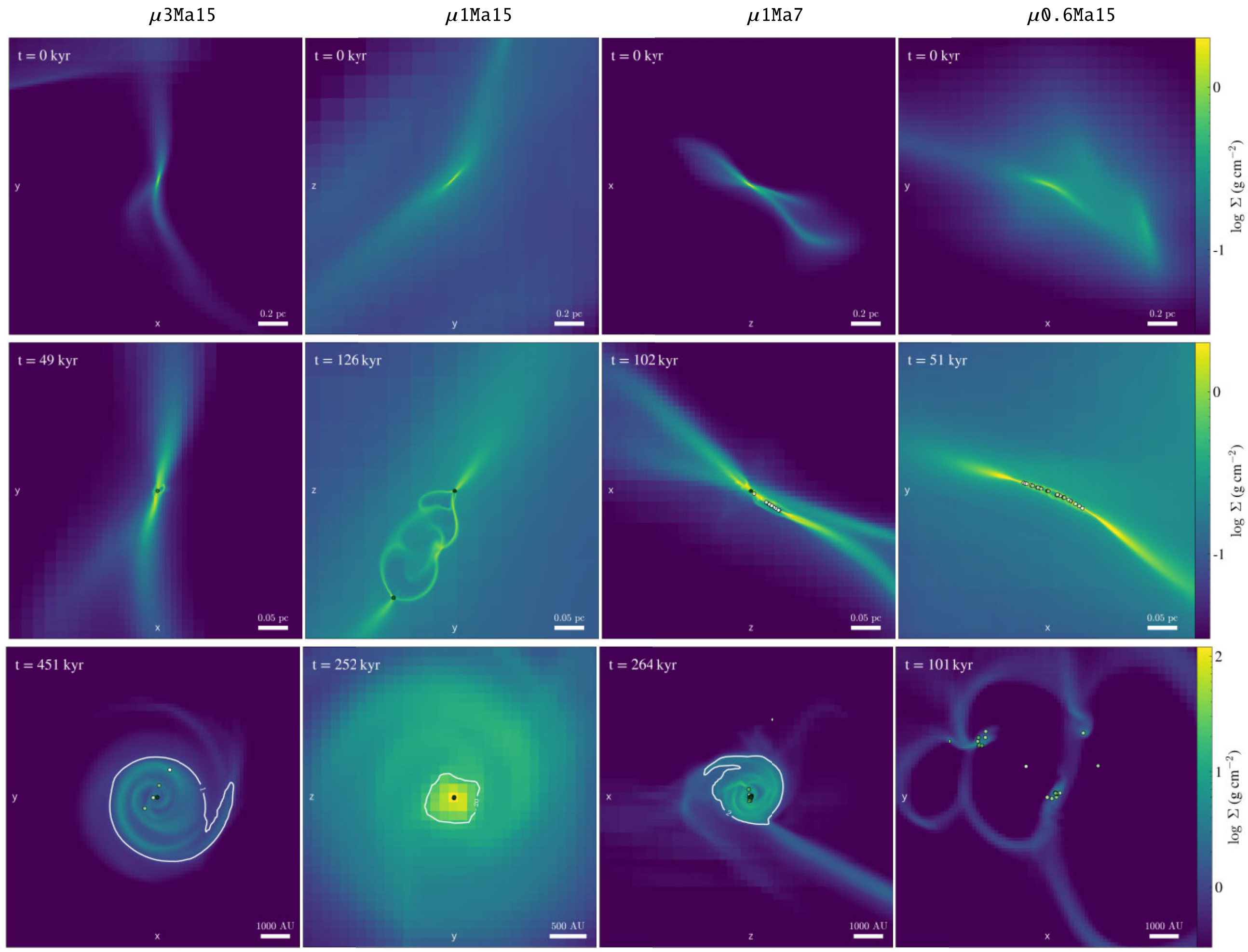

Figure 2. Surface density maps of the four cores (from left to right) inspected in Fig. 1, showing their time evolution (from top to bottom) and the formation of stars. The circles mark the positions of the sink particles which represent individual stars. The colours of the circles, from white to dark green, correspond to their masses from 0.1 to 10 $M_\odot$ in log scale. A large Keplerian disc forms in all cores in GMCs with $\mu_0 \gtrsim 1$. In the case where $\mu_0 < 1$ (μ`0.6Ma15`), the core collapses into a sheet-like shape with negligible angular momentum with respect to the centre of mass, preventing disc formation.

lines. In the weaker magnetic field cases (μ`3Ma15`, μ`1Ma15`, and μ`1Ma7`), the core collapses starting from a gas filament oriented perpendicular to the magnetic field lines. This nearly 1D structure is denser near its centre of mass and the density decreases in the outer parts of the filament. Both the surface density plots and the slice plots show similar morphology and orientation of the filament geometry, which is also confirmed by an inspection of the 3D rendering of the gas density (not shown in this paper). In the stronger magnetic field case (μ`0.6Ma15`), the gas also collapses along the field lines but into a 2D sheet-like structure. The gas surface density of the sheet is also not uniform, and the peak density defines a 1D curve, or filament, that is not necessarily oriented perpendicular to the B-field lines. This can be observed in the surface density plot for run μ`0.6Ma15` in Fig. 1, showing a filament structure apparently oriented along the B-field lines. However, the slice plot indeed shows the magnetic field lines threading through the sheet are perpendicular to its surface. To summarize, since the surface density is the quantity more readily observable, in the weak B-filed case the surface density maps reflect the actual filamentary shape of the gas leading to core formation. In the strongly magnetized cloud, however, the surface density map may lead observers to mistakenly think that the structure is a filamentary or disc-like structure rather than a 2D sheet structure.

During the next stage of collapse, the gas fragments along the filament or along the central high-density line of the sheet (Fig. 2). In the supercritical/critical ($\mu_0 \geq 1$) cases, the core fragments into multiple stars along the filament. Due to the conservation of angular momentum, the filament spirals inward and forms a Keplerian disc (Fig. 3). We discuss the disc properties in Sections 3.3 and 3.4. The fragments are ultimately embedded in the Keplerian disc, as already shown in our previous work (Paper I). In the cases where $\mu_0 < 1$, the sheet-like structure collapses towards the central high-density line. When the central density reaches the local Jeans density, the gas collapses to form numerous stars that are clustered into clumps. Due to magnetic braking, as will be discussed in Section 3.4, the angular momentum of the gas is transferred outward and the gas flows directly into the centre of the local clump without forming a disc.

To take a peek at how the magnetic field morphology evolves over time, we plot the magnetic field lines of core μ`3Ma7-hires` at three snapshots in Fig. 4. As the cores collapse, the magnetic field is bent by the rotation of the gas through the dynamo effect. The field lines are twisted and the magnetic strength is enhanced at the disc centre, which is also demonstrated by the 3D volume rendering of the magnetic field lines in Fig. 5. The field is dominated by the toroidal

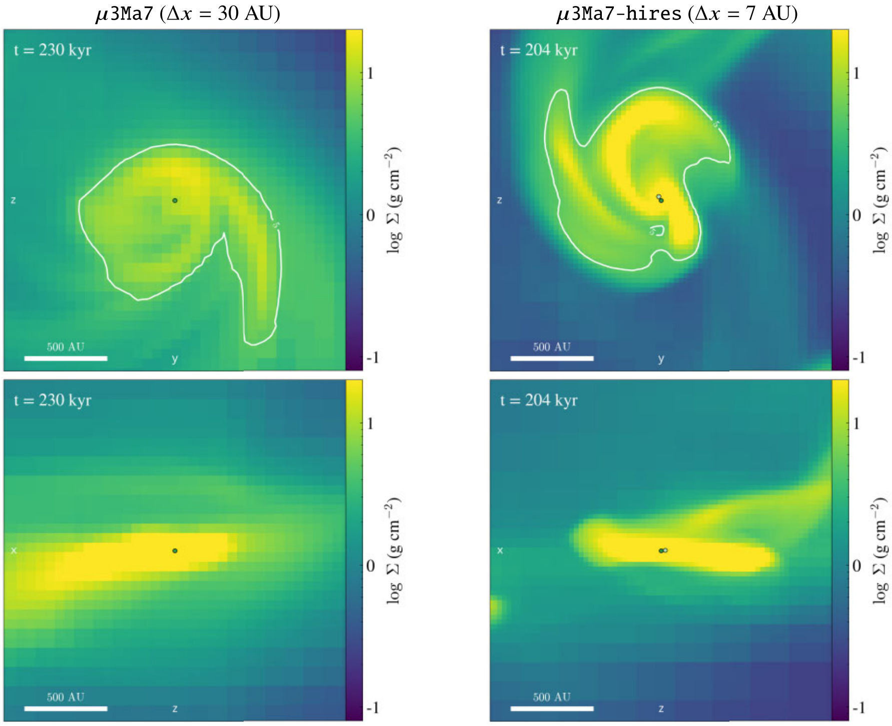

Figure 3. Face-on (top panels) and edge-on (bottom panels) view of the disc surface density in run μ3M7 (left) and its high-resolution counterpart (μ3M7-hires, right). Run μ3M7 has a spacial resolution of $\Delta x_{\min} = 30$au, while run μ3M7-hires has four times better resolution ($\Delta x_{\min} = 7$au). A white contour representing $\Sigma = 5$ g cm^{-2} is shown in the face-on view to indicate the disc contour. The similarity in disc structure and sizes between both runs suggests numerical convergence in the resolution of these large discs.

Table 2. Disc properties from simulations listed in Table 1. The columns are core names, disc radius (in au), disc thickness (in au), disc lifetime (in kyr), and number of sink particles formed in the vicinity of the disc that are either orbiting, ejected, or at the centre of the system. R and H represent the estimated average radius and thickness of the central, large disc during its lifetime.

Core name	R (au)	H (au)	t (kyr)	N_{sink}
μ3Ma15	1000	400	230	6
μ3Ma15-large	5000	3000	>500	9
μ1Ma15	300	100	>60	2
μ0.6Ma15	None	None	None	32
μ3Ma7	600	200	>100	3
μ3Ma7-hires	600	200	>100	12
μ1Ma7	1000	200	>10	21
μ0.6Ma7	None	None	None	112

component in the inner region and by the poloidal component in the outer region, which has implications on the strength of magnetic braking as will be discussed in Section 3.4.

3.2 B–ρ relationship

Understanding the relationship between density and magnetic field, as well as their physical origin, is crucial for both observations and theoretical models. According to simple models (e.g. Crutcher 1999), the magnetic field and gas density of a collapsing molecular cloud follow a power–law scaling relationship, $B \sim \rho^{\kappa}$. Assuming flux-freezing in ideal MHD, in the scenario of the isotropic collapse of a spherical cloud threaded by uniform parallel magnetic field lines, the relationships $B \propto R^{-2}$ and $\rho \propto R^{-3}$, imply $B \propto \rho^{2/3}$. In the scenario of the anisotropic collapse of a flattened structure or disc, the evolution of the gas collapse consists of two stages: during the first stage the cloud collapses along the field lines to form a disc. The gravitational acceleration at the disc surface, according to Gauss's law, is approximately $g \approx -2\pi G\Sigma$, where $\Sigma = \rho H = M/(\pi R^2)$ is the gas surface density, and H, R, and M are the disc thickness, radius, and mass, respectively. In the second stage, assuming flux-freezing, the mass-to-flux ratio $M/\Phi_B = \Sigma/B$ is conserved, therefore $B \approx \Sigma\Phi_B/M$. Assuming $g \approx \sigma^2/H$, i.e. the disc is supported by turbulent pressure in the vertical direction, we find $\sigma^2 \approx 2\pi G\rho H^2 \sim 2\pi G\Sigma^2/\rho$. Therefore,

$$B \approx \frac{\sigma}{\sqrt{2\pi}\ c_\Phi \mu}\rho^{1/2}, \tag{5}$$

or expressed in terms of the Alfven velocity

$$v_A = \frac{B}{\sqrt{4\pi\rho}} \approx \frac{\sigma}{2\sqrt{2\pi}c_\Phi\mu}. \tag{6}$$

An even simpler interpretation of this relation is the equipartition between magnetic and kinetic energy, $B^2/(4\pi) \propto \rho\sigma^2$, noting that

$$\frac{v_A^2}{\sigma^2} = \frac{1}{8\pi^2 c_\Phi^2 \mu^2} = \frac{0.45}{\mu^2}. \tag{7}$$

In flattened cores where μ is marginally greater than 1, this relationship predicts that magnetic pressure is slightly weaker than turbulent pressure.

Our discussion of the B–ρ relationship is organized into two regimes: the GMC scales and core scales. The former is the larger scale, encompassing all gas inside the simulation box that houses the GMC. The latter focuses on the more localized region of prestellar cores, specifically targeting the gas contained within an individual core.

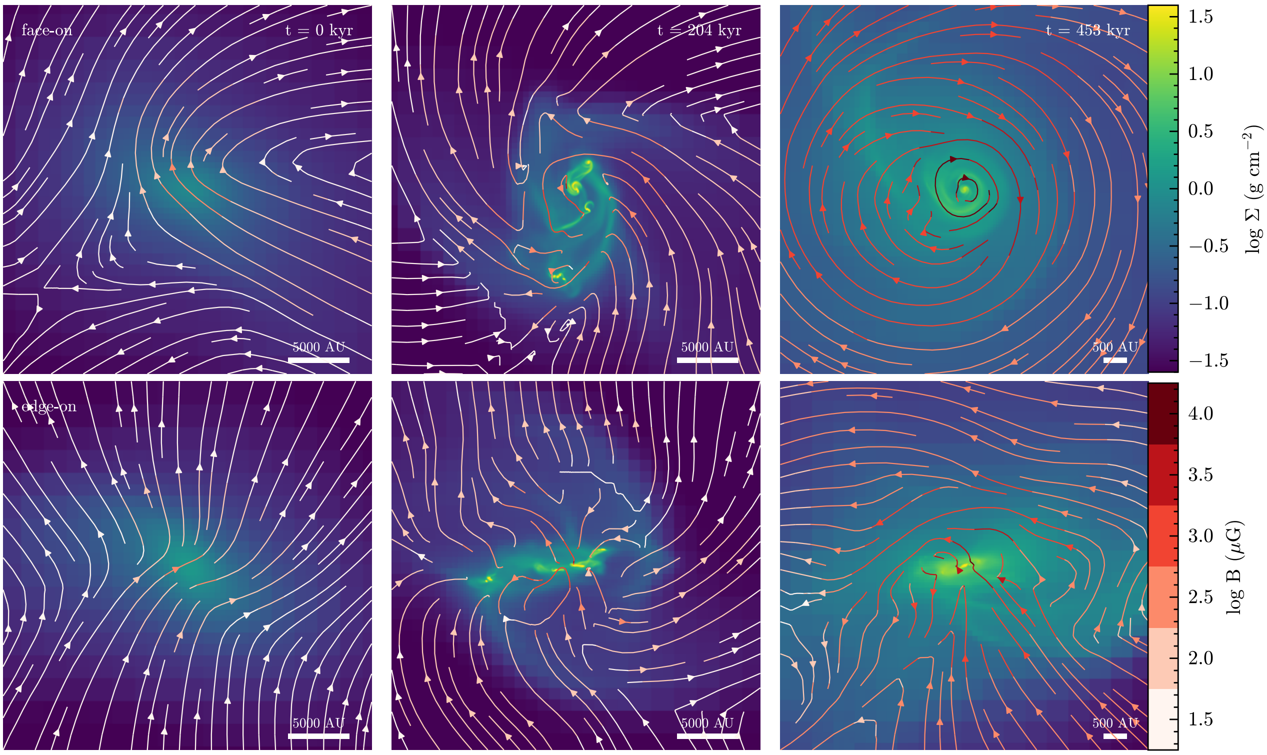

Figure 4. Temporal evolution (from left to right) of the magnetic field morphology of core μ`3Ma7-hires` in a face-on view (top row) and edge-on view (bottom row). Each panel shows gas column density centred at the peak density, overplotted with magnetic field streamlines. The colour of the streamlines shows the magnetic strength as indicated by the colourbar at the bottom right. A zoom view of the central disc is shown in Fig. 3. These streamlines show how the magnetic field lines are wound up as the disc forms and that the magnetic field is extremely turbulent, especially near the disc centre.

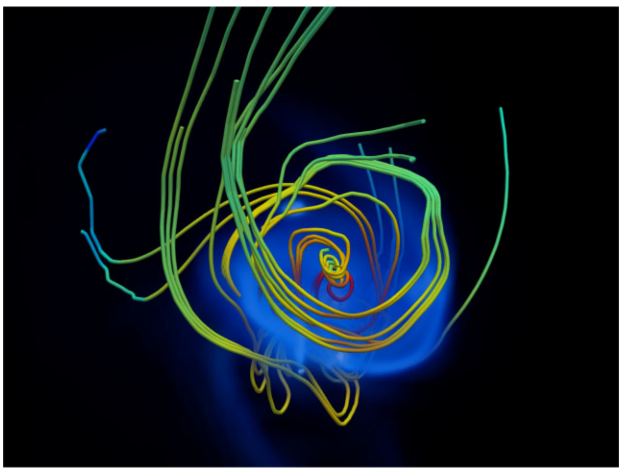

Figure 5. 3D view of the magnetic field lines on top of the volume rendering of the toroid around the central stars in run μ`3Ma7-hires`. The rendering in blue shows the density in this region above 10^6 cm^{-3}. The field of view measures 10 000 au. Note that the disc, about 600 au in radius, is at the centre and is much smaller. The tubes indicate the direction of the field lines and their colours indicate the strength of the magnetic field with red to blue meaning strong to weak.

3.2.1 *B–ρ relationship in GMCs*

It is well-established (Troland & Heiles 1986; Crutcher et al. 2010) that at low densities ($\lesssim 10^3$ cm^{-3}), the intensity of the magnetic field does not depend on gas density. This phenomenon is clearly seen in our simulations (Fig. 6), and this constant value of the magnetic field is the same as the B_0 set in our initial conditions. At higher densities, up to $\sim 10^9$ cm^{-3}, the magnetic field scales with density as $B \propto \rho^{1/2}$, resulting in a universal value of the Alfven velocity of $v_A \sim 0.5 \pm 0.1$ km s^{-1}. In Fig. 6, we show phase plots of B vs gas number density n for GMCs with a range of μ_0 from 3 to 0.6 and for turbulent Mach numbers $\mathcal{M} = 7$ and 15. The red line, showing the mass-weighted average of B at a given n, suggests that the Alfven velocity derived from this median relationship is nearly constant independently of μ_0 and $\mathcal{M}$. It is important to note, however, that the Alfven velocity is only approximately constant above the critical density, and the exact value may also depend on other cloud properties. In Section 3.2.3, we will explore the physical mechanisms that govern the scaling of the magnetic field with density in more detail.

Given a background magnetic intensity B_0, we can estimate from Fig. 6 the critical gas density at which the Alfven velocity equals the universal value $v_A = 0.5$ km s^{-1}:

$$n_{\rm cr} \equiv \frac{1}{4\pi \mu m_{\rm p}} \left(\frac{B_0}{v_A}\right)^2 \approx 2.2 \times 10^4 {\rm cm}^{-3} \left(\frac{B_0}{30\mu G}\right)^2, \tag{8}$$

where $\mu = 1.4$ is the mean molecular weight and m_p is the proton mass. For the B_0 values in our simulations, ranging from 10 to 50μB, the critical density falls within 2.5×10^3 to 6×10^4 cm^{-3}. This range is roughly consistent with the lower end of the core density in our simulations, suggesting that cores form when the magnetic field is no longer strong enough to support the cloud against gravitational collapse.

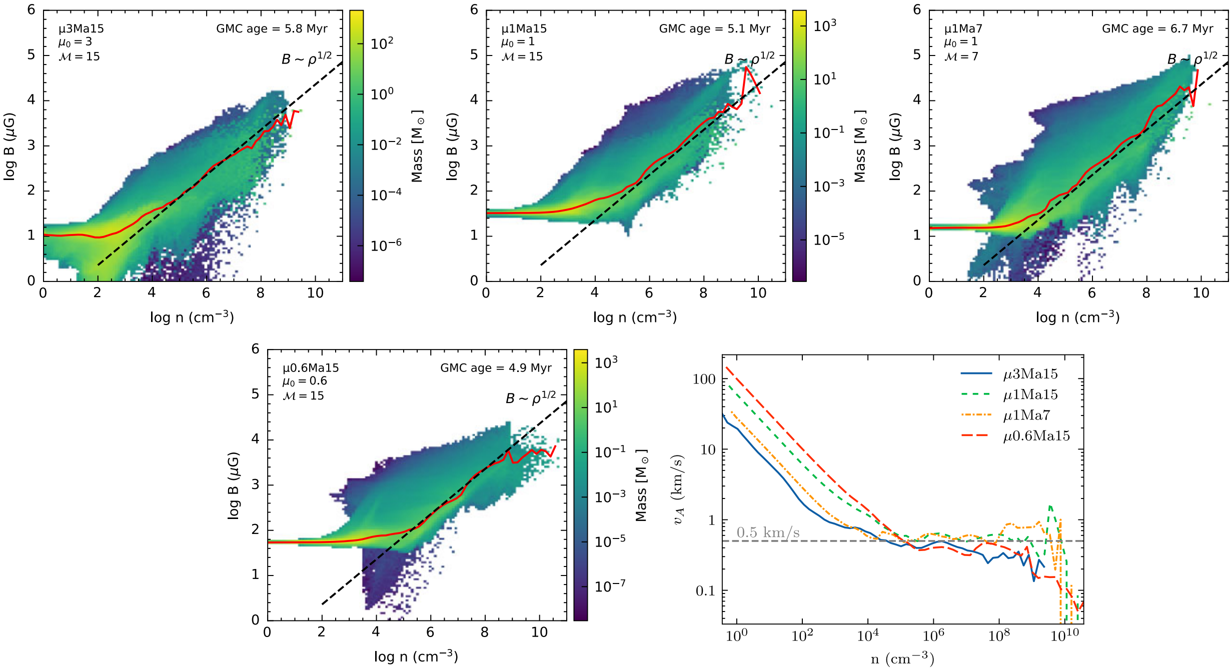

Figure 6. The global B–ρ relationship at GMC scales for the μ`3Ma15`, μ`1Ma15`, μ`1Ma7`, and μ`0.6Ma15` runs. At low density ($\lesssim 10^3$ cm^{-3}), the magnetic field intensity is independent of the density and the global value is determined by the initial magnetization. At high density up to $\sim 10^9$ cm^{-3}, we find a universal B–ρ relation: $B \approx 86\ \mu$B $(n/10^5\ \mathrm{cm}^{-3})^{1/2}$, corresponding to a constant Alfven velocity of ~ 0.5 km s^{-1}. The first four panels show the 2D phase diagram of magnetic intensity B versus gas number density n of the four clouds, respectively, and the colours represent the gas mass. The red curves are the mass-weighted 1D relationship. The last panel plots the Alfven velocity v_A as a function of n, converted from the 1D $B - n$ relationship for all four clouds.

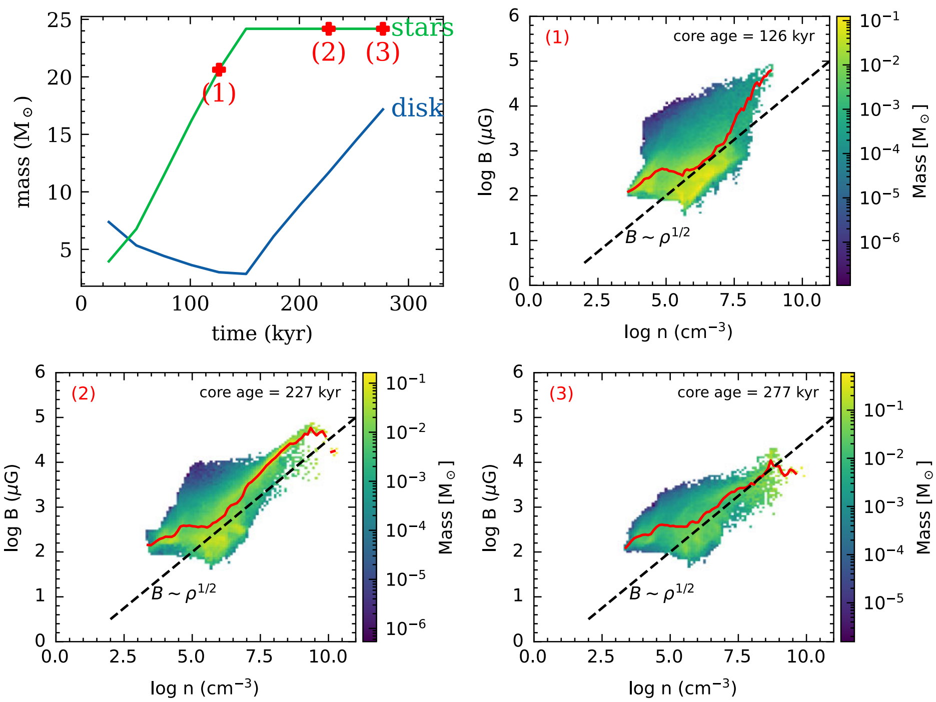

Figure 7. Enhancement of the magnetic intensity at high density inside the core μ`1Ma15`. The first panel shows the temporal evolution of the mass in stars and in discs. The rest of the panels show a 2D phase diagram of $B - n$, similar to Fig. 6, inside the core at various times as marked in the first panel. We show that as the gas is accreted by sink particles while the magnetic field is retained outside, the magnetic intensity is boosted by nearly an order of magnitude at a density above 10^7 cm^{-3}. As the accretion stops, the strong magnetic field disperses itself due to magnetic pressure/tension.

3.2.2 B–ρ relationship in cores

In Fig. 7, we show the B–ρ relationship for gas in the cores of the zoom-in simulations. In the cores, the gas with density lower than $10^7\mathrm{cm}^{-3}$ approximately follows the same universal relationship $B \propto \rho^{1/2}$ with the same normalization as at GMC scales (Fig. 6). However, at densities $> 10^7$ cm^{-3} we notice that the magnetic field intensity at a given density is enhanced with respect to the universal value when the sink particle accretes gas. This phenomenon is likely a result of the release of the magnetic field during sink accretion, as the sink particles accrete gas but not magnetic field, hence the conservation of mass-to-flux ratio, valid in ideal MHD, is broken within the sink particles. This recipe for sink accretion is mainly motivated by the fact that, while preserving the divergence-free condition ($\nabla \cdot B = 0$) is essential for the stability and accuracy of MHD simulations, accreting magnetic flux on to sink particles while maintaining this condition is currently not possible with existing numerical methods (see a review of Teyssier & Commerçon 2019). This is also particularly inspired by the magnetic flux problem in star formation: the mass-to-flux ratio in a star is 10^{5-8} times higher than that at the cores' scale. The slope of the B–ρ relation at densities $> 10^7$ cm^{-3} is close to 2/3, suggesting that the collapse at disc centre is nearly isotropic. The boost in the B field at a given ρ persists as long as the sink particle is accreting gas. Shortly after the accretion stops, the magnetic field strength reduces back to the average value following the global B–ρ relationship. Evidently, the accumulation of B-field lines in the sink produces a temporarily stronger magnetic pressure diffusing the magnetic field lines outward (Zhao et al. 2011).

3.2.3 Interpretation of the universal B–ρ relationship

In all the phase plots we observe two regimes: (A) a low-density regime where the mean of the magnetic field is constant as a function of ρ, even though the spread around the mean can be large, especially for weaker values of the initial B-field (large μ cases); (B) a high-density regime, where $B \propto \rho^{1/2}$, or $v_A = \mathrm{const}(\rho)$. These two regimes are observed for the GMC as a whole (in this case the constant B value is the one set in initial conditions), and for individual cores: in this second case the constant B value regime is the one at the boundary of the core where the density is lowest.

The regime (A) is the case when the density of the gas can increase or decrease while leaving B constant: this happens when the motion of the gas is along the magnetic field line. For instance, the initial turbulent motions of the gas can compress or de-compress the gas: when the gas is compressed (de-compressed) in the direction of the magnetic field lines, B remains the same but the density increases (decreases). If the motion is perpendicular to B, the value of B can increase or decrease for compression/decompression. However, this will just produce a constant scatter in the B–ρ relationship around the mean if there is no preferred direction for the turbulence (isotropic turbulence). We expect the scatter around the mean to be small for smaller $\mathcal{M}$ or smaller μ, as the stronger magnetic tension/pressure relative to the amount of turbulence suppresses compression/de-compression perpendicular to the B-filed direction. This is indeed observed in Fig. 6: in regime (A), where $B \sim \mathrm{const}(n)$ (at densities $n < 10^3$–10^4 cm^{-3}), the scatter of the B-field at a given density is larger for the first panel (top left) with respect to all the other cases. The simulation in the top left panel has the largest Mach number and the lowest initial magnetic field strength, providing support to our interpretation.

This regime no longer exists at cores scales (high densities) when the gas motion is no longer isotropic, rather it is mostly compression due to the self-gravity of the cores under the influence of strong magnetic field. Assuming that cores can be initially approximated as isothermal spheres embedded in a uniform magnetic field supported by thermal and turbulent pressure in the direction of the magnetic field lines, one can apply the derivation in Section 3.2 and equation (7). After the initial phase of compression in the z-direction at constant Σ and B, any further density increase is produced by compression perpendicular to the B-field lines, producing $B \propto \rho^{1/2}$ or $v_A = \mathrm{const}(\rho)$. But what sets the constant value of $v_A \sim 0.5$ km s^{-1} observed across different scales and densities?

The values of σ and μ in equation (7) are not the initial values for the GMC, but rather the initial values for self-gravitating cores. If the cores are in quasi-hydrostatic equilibrium supported by turbulence and magnetic pressure, $W \sim (\mathcal{B} + K_{\mathrm{turb}})$. If the initial value of the magnetic pressure is comparable to or dominates over turbulence we expect $\mu \equiv \sqrt{|W/\mathcal{B}|} \sim 1$. Assuming that the core is marginally Jeans unstable and partially supported by turbulent pressure, the equivalent Jeans mass is given by

$$M_J = \frac{\pi^{5/2}}{6} \frac{\sigma^3}{(G^3\rho)^{1/2}}, \tag{9}$$

where σ is the rms of the turbulent velocity. In GMC simulations by He et al. (2019) the typical masses of prestellar cores (the most numerous cores in the core mass function) is $M \approx 1$–$5\ \mathrm{M}_\odot$, and $n = 10^7$ cm^{-3} is their typical gas number density. Using these values in equation (9) we get $\sigma \approx 0.6$ km s^{-1}. Note that the same value can be obtained by calculating the virial velocity of the core. Finally, using equation (7) with $\mu \sim 1$ we have $v_A \approx 0.67\sigma \approx 0.4$ km s^{-1}, in agreement with the mean value for the whole GMC and for individual cores. Because σ is weakly dependent on M_J and the core mass function in the GMC is dominated by small-mass cores with $M \sim 1$–$5\ \mathrm{M}_\odot$, most of the dense gas in the GMC is in cores with $\sigma \sim 0.6$ km s^{-1}. Therefore, in the high-density regime $v_A \approx 0.4$ km s^{-1} when averaged over the whole cloud. Note, however, that our most massive cores have $M \sim 130\mathrm{M}_\odot$. Indeed, the B–ρ phase diagram for the most massive core in our set (μ`3Ma15-large`) shows higher values of v_A, consistent with our interpretation.

3.3 Magnetic and turbulent support in the cores and discs

The cores initially have nearly critical magnetic field strengths, with values of the mass-to-flux ratio, $\mu(r)$, ranging from 0.5 to 3 from the inner to the outer part of the core (see the top row in Fig. 8). The μ radial profiles in cores that form from GMCs with different initial magnetic field strengths are virtually indistinguishable from each other: the mass-to-flux ratio in the μ`0.6Ma7` core is only slightly lower than that in the μ`3Ma7` core. This is likely due to a selection effect because magnetically sub-critical 'clumps' would fail to collapse and form a sink particle. During the quasi-spherical initial collapse of the cores, the magnetic pressure ($\propto \rho v_A^2$) dominates over the turbulent ($\propto \rho\sigma^2$) and thermal pressure ($\propto \rho c_s^2$).

As discussed in Section 3.2, the prestellar core collapses anisotropically to form a disc structure. During this transition, while the magnetic flux remains roughly unchanged, the total magnetic energy in the gas decreases as the gas volume decreases, whereas its gravitational energy increases. Consequently, the mass-to-flux ratio μ, as defined in equation (3), increases. This is evident in the top row of Fig. 8, where the mass-to-flux ratio in the disc (forming at later

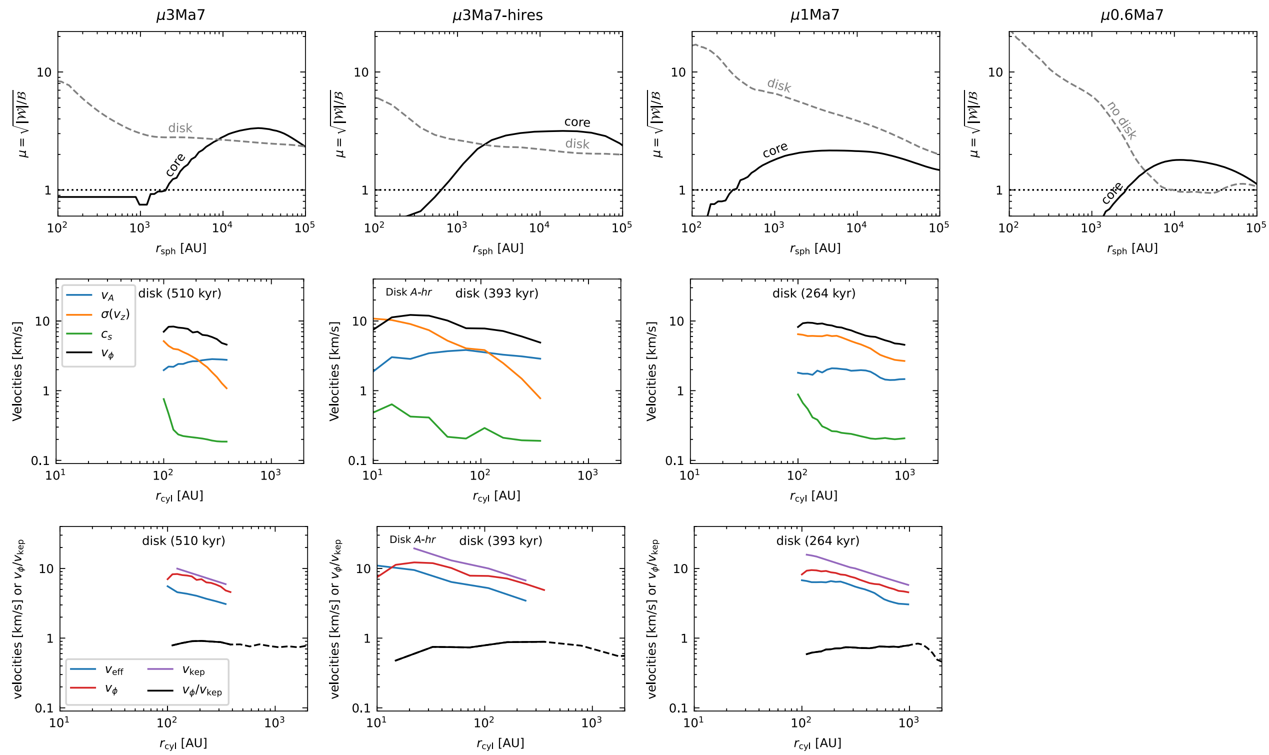

Figure 8. The magnetic, turbulent, and thermal support of the cores and discs. From left to right are the cores μ3Ma7, μ3Ma7-hires, μ1Ma7, and μ0.6Ma7. Row 1: the mass-to-flux ratio radial profile of the gas at the core phase (initial time $t = 0$) and disc phase (later stage, and the exact time is shown in rows 2 and 3) as a function of radius. Row 2: radial profiles of the mass-weighted Alfven velocity, z-component turbulent velocity, sound speed, and the effective velocity of support $v_{\rm eff} = (v_A^2 + \sigma(v_z)^2 + c_s^2)^{1/2}$ during the disc phase as a function of the radius in cylindrical coordinates. Row 3: radial profiles of the mass-weighted effective velocity, the azimuthal velocity, the Keplerian velocity, and the Keplerianity $\beta_K = v_\phi/v_{\rm kep}$ during the disc phase as a function of the radius in cylindrical coordinates. In rows 2 and 3, only disc material is included in the calculations, with the envelope excluded. The profiles are shown starting at half the sink accretion radius (defined as $4\Delta x_{\rm min}$). Caution should be taken when interpreting the region below the sink accretion radius. The $v_\phi/v_{\rm kep}$ curve is extended beyond the disc radius (indicated by the dashed line) to illustrate the trend of Keplerianity in the toroid. Quasi-Keplerian discs with $v_\phi \approx v_{\rm kep}$ extending to radii $r_{\rm cyl} \sim 300$–1000 au form in all runs except μ0.6Ma7. The cores are initially supported by magnetic pressure, while thermal and turbulent pressures play sub-dominant roles. The toroids forming in the cores are supported by both turbulent and magnetic pressure, with the former slightly dominating in the quasi-Keplerian discs found in the inner part of the cores ($\lesssim$ 1000 au) and the latter slightly dominating in the outer part (toroid). Thermal support is negligible in all the massive cores analysed in this study.

times than the core) is approximately one order of magnitude higher than that in the core (defined at $t = 0$).

In the bottom two rows, we plot the disc profile as a function of the cylindrical radius $r_{\rm cyl}$. The disc remains quasi-Keplerian ($v_\phi \approx v_{\rm kep}$) up to a characteristic radius of about 1000 ± 500 au in all the cores but the sub-critical one with $\mu = 0.6$: in this run $v_\phi << v_{\rm kep}$ at all radii and a Keplerian disc fail to form (see Fig. 2).

As the core collapses, the turbulence is amplified, particularly in the inner parts of the disc/core. In the outer disc, turbulent kinetic energy and magnetic energy are nearly in equipartition. Within the disc, the Alfven velocity (v_A) remains around 1 km s^{-1}, occasionally increasing to 5 km s^{-1} in the inner part. The effective velocity, $v_{\rm eff}^2 = v_A^2 + \sigma^2 + c_s^2$, consistently approaches the Keplerian velocity within the disc radius but falls significantly below $v_{\rm kep}$ outside the disc radius. While the exact cause of the increased turbulence remains unclear, the most plausible explanation is non-axisymmetric accretion, given the highly asymmetric nature of the inflow. In our simulations, the accretion of material on to the disc is highly irregular and asymmetric, especially during the later stages of core collapse (see Figs 2 and 3), introducing significant perturbations in the disc structure and potentially amplifying turbulence to a level where the turbulent velocity is close to the escape velocity. Unlike axisymmetric accretion, where material is smoothly added to the equatorial plane, as seen in the evolution of an isolated core, non-axisymmetric accretion delivers mass and angular momentum unevenly. This creates localized pressure gradients and velocity shears, which disrupt the smooth gas flow and drive turbulent motions both in the surrounding toroid and within the disc.

The grey-dashed lines in the top row of Fig. 8 show the μ profiles of the discs at the same time point as the curves shown in the last two rows. The discs have $\mu(r) \sim 10$ in the inner parts where turbulent support is dominant, but $\mu(r)$ decreases to ~ 2 in the outer envelope. This decrease of $\mu(r)$ in the outer parts of cores has already been observed: Yen et al. (2023) has shown that the mass-to-flux ratio increases from 1–4 to 9–32 from 0.1 pc to 600 au scales, which suggests that the magnetic field is partially decoupled from the neutral matter from large to small scales. The authors suggest non-ideal MHD (e.g. ambipolar diffusion) as the cause of this μ radial profile that allows the formation of a Keplerian disc. In our simulations, modelling of non-ideal MHD processes is not included in our equations, other than indirectly in our recipe for sink accretion: sinks accrete mass, momentum, and angular momentum but not magnetic field. Hence, a deviation from flux-freezing is caused by the accumulation and subsequent diffusion of the magnetic field (Zhao

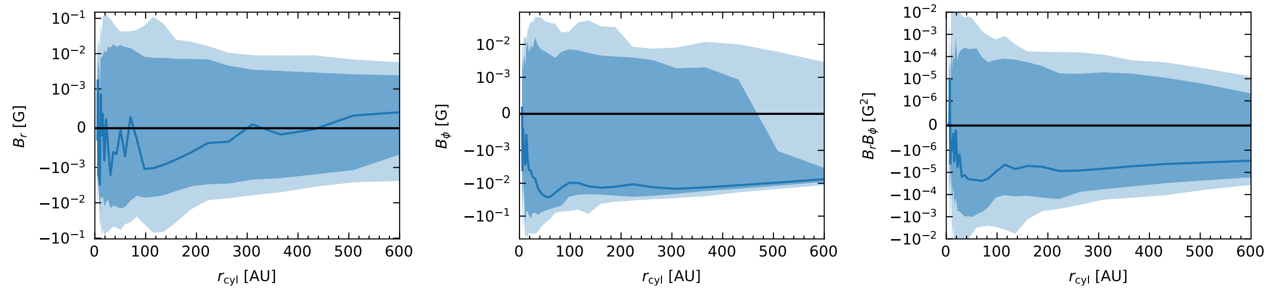

Figure 9. Explanation of the weak overall magnetic braking in disc μ`3Ma7-hires`. From left to right are the distributions of the radial component of the magnetic field, the azimuthal component of the magnetic field, and their product, which is proportional to $t_{\rm br}^{-1}$, as a function of disc radius in cylindrical coordination. The time at which the analysis is done is 393 kyr after the core formation, the same as that in Fig. 8. The thick curve displays the median values and the shaded area displays the 1σ and 3σ contours for the probability distribution function. While the azimuthal component of the magnetic field is predominantly directional, the radial component exhibits significant turbulence and incohenrence. The positive and negative values of $B_r B_\phi$ (and consequently $t_{\rm br}$) from cell to cell tend to cancel cancel each other out, resulting in a small overall magnetic braking effect.

et al. 2011; Santos-Lima et al. 2012) within sink particles described before. The increase of μ in the inner part is mainly produced by the increase of the gravitational potential energy $|W|$ from the mass increase of the sink particle which, however, does not accumulate magnetic energy.

3.4 Magnetic braking problem

As discussed before, the formation of a toroid or a disc can be suppressed or its radius reduced by magnetic braking. The spinning of the gas twists up the magnetic fields, creating a tension force that opposes rotation. The magnetic field exerts a Lorentz force per unit volume on the fluid element which, at a given radius r, can be written as

$$\mathbf{f} = \frac{1}{4\pi}\left[(\nabla\times\mathbf{B})\times\mathbf{B}\right] \quad (10)$$

$$= \frac{1}{4\pi r}\left[\mathbf{B}_p\cdot\nabla_p(rB_\phi)\right]\hat{\phi} \quad (11)$$

$$= \frac{1}{4\pi}\left(B_rB_\phi + rB_r\frac{\partial}{\partial r}B_\phi + rB_z\frac{\partial}{\partial z}B_\phi\right)\hat{\phi} \quad (12)$$

$$\approx \frac{B_rB_\phi}{4\pi}\hat{\phi}, \quad (13)$$

where the subscript p denotes the poloidal component of the filed and $\nabla_p = (\frac{\partial}{\partial r}\hat{r}, \frac{\partial}{\partial\phi}\hat{\phi})$. We have only considered the ϕ component of the torque and assumed that the gradient of B_ϕ to the z-direction vanishes due to symmetry at the equatorial plane of the disc. The second term in the parenthesis of equation (12) is negligible compared to the first term for a B-field with a azimuthal component that is nearly constant as a function or radius (i.e. $d\ln B_\phi/d\ln r < 1$). Therefore, we have

$$\frac{\mathrm{d}}{\mathrm{d}t}(\rho v_\phi) = -\frac{|\mathbf{f}|}{r} \approx -\frac{B_rB_\phi}{4\pi r}. \quad (14)$$

The magnetic braking time is defined as the characteristic time-scale for the magnetic torque to remove completely the gas angular momentum:

$$t_{\rm br} = \frac{\rho v_\phi}{-\frac{\mathrm{d}}{\mathrm{d}t}(\rho v_\phi)} \approx \frac{4\pi\rho v_\phi r}{B_rB_\phi}. \quad (15)$$

To compare $t_{\rm br}$ with the dynamic time-scale, we assume $B_rB_\phi \approx B^2$ and get

$$t_{\rm br} \approx \frac{4\pi\rho v_\phi r}{B^2} = \left(\frac{v_\phi}{v_A}\right)^2\frac{r}{v_\phi} = \left(\frac{v_\phi}{v_A}\right)^2 t_{\rm cr}. \quad (16)$$

This means that if a cloud has a magnetic field nearly in equipartition with gravitational potential energy and if the field is marginally wound up such that the poloidal and toroidal components become comparable, we expect $t_{\rm br}\sim t_{\rm cr}$, i.e. the field is capable of stopping Keplerian rotation in a time-scale of the order of the disc rotation period. For instance, at $r = 400$ au in the disc of core μ`3Ma7`, $v_\phi \approx 5\ {\rm km\,s^{-1}}$, $v_A \approx 2.5\ {\rm km\,s^{-1}}$, and $t_{\rm cr} = 0.4$ kyr. From equation (16) we have $t_{\rm br}\approx 4t_{\rm cr}\approx 1.6$ kyr that is significantly shorter of the disc lifetime $\gtrsim 300$ kyr. A time-scale $t_{\rm br}$ a factor of 2 times longer is obtained if we assume $B_rB_\phi \approx B^2/2$.

At least for the massive discs studied in this work, which are supported in the vertical direction by (supersonic) turbulent motions rather than thermal pressure, we argue that apparently contradictory results regarding the time-scale for magnetic braking and the critical μ value suppressing disc formation can be understood in terms of the turbulent and incoherent nature of magnetic fields in massive cores/toroids. In Fig. 9, we plot the distribution of the toroidal and poloidal components of the magnetic field, B_ϕ and B_r, in the cylindrical coordinate at a given distance to the disc centre for core μ`3Ma7-hires`. The coordinate system is the same as that defined in the previous section. At a given radius in the cylindrical frame, we pick all the cells in a concentric and superposed ring and compute each component of the B field weighted by gas mass. The median, $1-\sigma$, and $3-\sigma$ contours for the distribution of the radial component, B_r, the azimuthal component, B_ϕ, and their product are then plotted in the three panels. We can see that while the azimuthal component of the magnetic field is mostly directional, the radial component, on the other hand, evenly scatters around zero. In Fig. 10, we plot the radial profile of the volume-weighted mean and rms of B_ϕ, $B_{\rm r}$ and $B_{\rm r}B_\phi$ for discs μ`3Ma15`, μ`3Ma7`, and μ`1Ma7`. As we can see, the radial component B_r in all the discs is extremely turbulent, and the turbulent root-mean-square (rms), $< B_r^2 >^{1/2}$, is roughly $10\times$ higher than the mean (second row). Consequently, the magnetic torque, proportional to B_rB_ϕ, scatters around zero. This results in the torque exerted on the gas cancelling itself out, greatly weakening the magnetic braking effect. This reduction of roughly a factor of 10 of the torque (bottom row) increases the braking time-scale $t_{\rm bf}$ by the same factor, ultimately influencing the longevity and stability of the discs compared to the case where the magnetic field lines are perfectly coherent and aligned with the spin axis of the disc/core. Furthermore, this reduction factor in the inner disc is several times higher than in the outer disc due to enhanced turbulent velocities (Fig. 8). Consequently, while the outer region

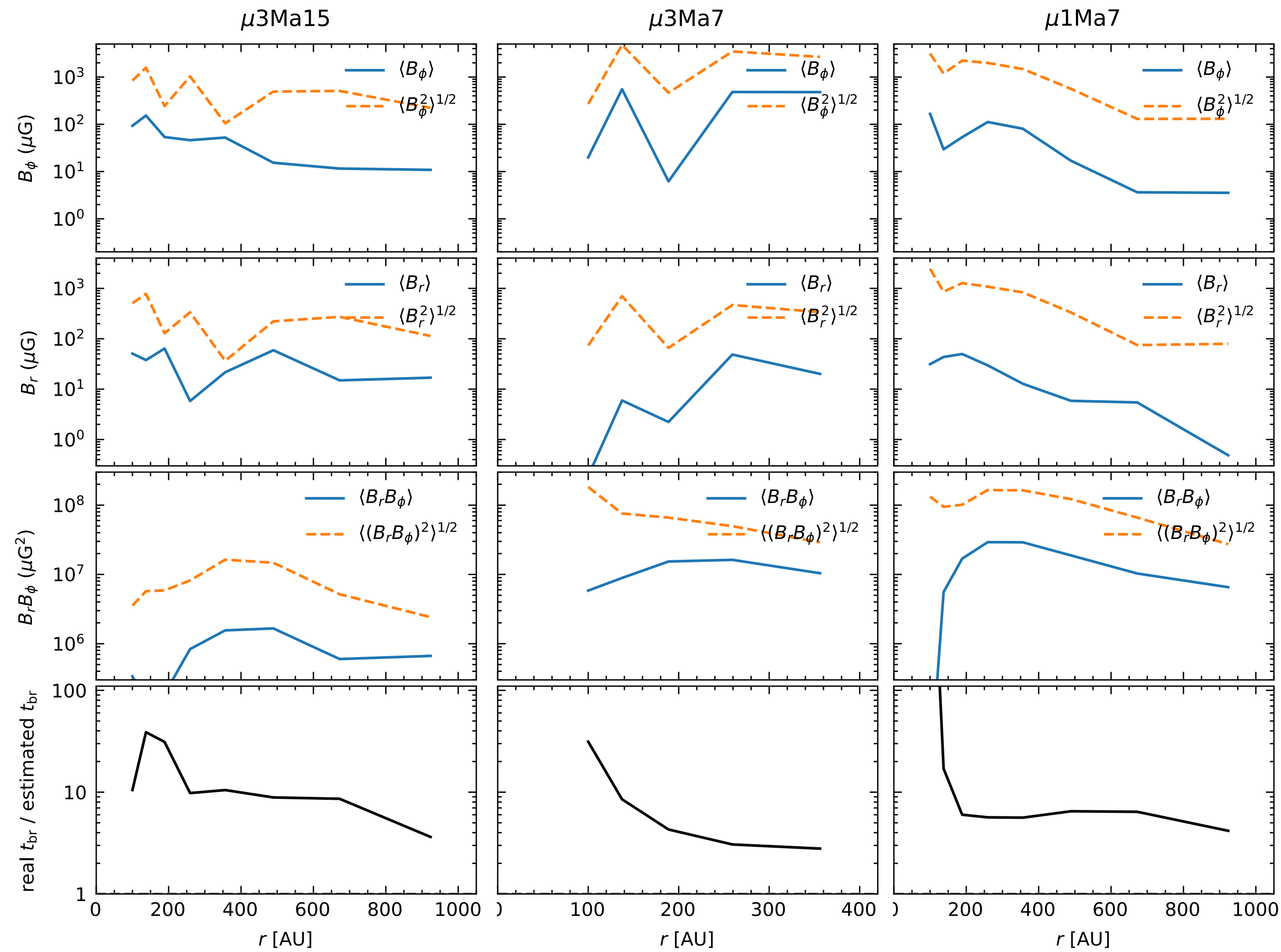

Figure 10. The extremely turbulent and incoherent magnetic field on the circumstellar discs as a solution to the magnetic braking problem. The columns from left to right are the diss from three cores with their label shown at the top. The time at which the analysis is done is the same as the discs in Fig. 8 (bottom two rows). Top row: the mean and standard deviation of the azimuthal component of the B field as a function of the cylindrical radius. Second row: the mean and standard deviation of the radial component of the B field. Third row: the mean and standard deviation of the products of the azimuthal and radial components of the B field. Bottom row: The ratio of the magnetic braking time, $t_{\rm br} \propto |\langle B_r B_\phi \rangle|^{-1}$, to the naive estimation, proportional to $\langle (B_r B_\phi)^2 \rangle^{-1/2} \approx \langle B^2 \rangle^{-1}$.

of the disc (beyond ~ 200 au) eventually experiences braking by magnetic fields, the inner part of the disc can persist for a longer duration.

We also notice that this incoherent character of the magnetic field does not significantly depend on the initial turbulence of the GMC, which ranges from $\mathcal{M} = 7$ to 15, nor on the magnetic strength, which ranges from marginally supercritical to critical ($1 < \mu < 3$). We also rule out resolution effects as a cause for the formation of large discs (Fig. 3).

4 DISCUSSION

The exponent of 1/2 we find for the B–ρ power–law relationship in the range of densities between 10^5 and 10^9 cm^3 indicates that the cloud collapse at these relatively large scales (compared to protostellar core scales, i.e. $> 10^4$ au) have cylindrical/filamentary geometry rather than spherical. This is true across all GMCs in our sample, irrespective of whether the turbulent energy is the dominant support against gravity ($\mathcal{M}_A = 5$ case) or the magnetic energy dominates ($\mathcal{M}_A = 1$ case). Our findings seem in contrast with the conclusion of a previous study by Mocz et al. (2017), which proposed that the collapse is isotropic ($B \propto \rho^{2/3}$) in environments when turbulence dominates over the magnetic field and transitions into anisotropic when the magnetic energy dominates. We identify two main factors contributing to this discrepancy. First, the range of densities investigated differs; our analysis spans up to 10^9 cm^{-3}, whereas Mocz et al. reached densities around 10^{11} cm^{-3}. Secondly, the authors point out that the B–ρ relation, when measured on a cell-by-cell basis – a method more akin to ours – exhibits a flatter power-law slope.

4.1 Previous ideal-MHD calculations of massive core collapse

A fundamental difference between hydrodynamic and magneto-hydrodynamic prestellar cores comes from the evolution of angular momentum. In the absence of a significant magnetic field, the angular momentum is essentially conserved and becomes a dominant support against gravitational collapse, drastically affecting the evolution of the cores. In a magnetized core, however, the situation is different; angular momentum can be exchanged between fluid particles because of magnetic force/tension. In the aligned configuration between the magnetic field and the cloud rotation axis, the magnetic braking time can become so short that the formation of the centrifugally supported discs can be even entirely prevented.

Recent numerical studies have explored how magnetic configurations/geometries, i.e. misalignment, may reduce the power of magnetic braking in low-mass (less than ~ 3 solar mass) cores. Hennebelle & Ciardi (2009) report the first discovery that centrifugal discs more easily form in 1 solar mass cores in which the magnetic field and the angular momentum vector are misaligned. Joos et al. (2012), Li et al. (2013b), and Hirano et al. (2020) report more quantitative results that are consistent with Hennebelle & Ciardi (2009). Joos et al. (2012) show that, in the case where the magnetic field and angular momentum are perpendicular to each other, the mean specific angular momentum of the central region of a core is about two times larger than that in the parallel case. Tsukamoto et al. (2018), however, claim that in the prestellar collapse phase, the presence of misalignment seems to enhance the angular momentum removal from the central region due to stronger magnetic braking, contradicting before-mentioned works. Future observations should be able to provide more evidence to disentangle this apparent discrepancy between simulation results.

Several studies have investigated the effects of turbulent magnetic fields on disc formation from intermediate- to high-mass cores (e.g. Seifried et al. 2013; Joos et al. 2013; Li et al. 2014; Fielding et al. 2015; Gray et al. 2018). For example, Joos et al. (2013) explored the impact of turbulence with high resolution and suggested that the impact of turbulence is limited. None the less, the correlation between turbulence and disc formation remains inconclusive. In a review article, Tsukamoto et al. (2023) argue that turbulent diffusion, whether as a numeric effect or non-ideal MHD effect, may not significantly influence the evolution of circumstellar disc sizes.

The calculations we present here extend the investigation of star formation under ideal MHD in two major ways beyond the studies mentioned above. Unlike in most of the above MHD simulations, which typically track the collapse of clouds below $100\mathrm{M}_\odot$, our work zoom-in at high resolution (tens of au) a few 30–100 $\mathrm{M}_\odot$ cores within the realistic environment of a much larger GMC. Specifically, we model the formation of massive prestellar cores, with masses between tens to one hundred solar masses, emerging from the collapse of GMCs with masses $\sim 10^4\mathrm{M}_\odot$ and different level of magnetization and turbulent energy. Despite of the computational challenges posed by simulating such large masses, we achieve a relatively high spatial resolution (between 10 and 60 au), sufficient to resolve discs with radii $\gtrsim 200$ au, and densities $\gtrsim 10^9\mathrm{cm}^{-3}$. The second innovation of our study is the adoption of realistic initial and boundary conditions that accurately captures the thermal, turbulent, and magnetic energy configurations essential for comparing their relative roles in the star formation process. Because our setup differs in mass scale and boundary/initial condition from most previous studies, we find results that at times seem to contradict previous results established in the literature. For instance, we find that large ($R \sim 300$–1000 au), rotationally supported discs can indeed form from the ideal-MHD collapse of prestellar cores, even under conditions where the cores are magnetically near-critical or critical. We motivate this result as due to the highly turbulent nature of the magnetic field within the discs, which are supported in the vertical direction by turbulent motions rather than thermal pressure. This is also contrary to previous findings for smaller mass discs that instead are supported by thermal pressure.

4.2 Previous non-ideal MHD simulations of massive core collapse

Non-ideal MHD effects may play a crucial role in shaping the evolution of discs, impacting their size through the decoupling of magnetic fields and gas, thereby reducing the magnetic braking efficiency within the disc (see Tsukamoto et al. 2023, for a review). First of all, relying solely on Ohmic dissipation proves insufficient in driving the formation of large circumstellar discs during the Class 0 phase (the first protostellar objects observed post-collapse within prestellar cores; Machida et al. 2011). This limitation arises from the fact that to significantly diffuse magnetic fields, Ohmic heating would elevate the core's inner region's temperature to a level where thermal energy matches gravitational energy, hindering the collapse of the core as a whole.

Ambipolar diffusion is a more effective magnetic diffusion process that weakens the effects of magnetic field in the disc and envelope of a protostar by allowing the ions to slip past the neutrals. 3D simulations have shown that ambipolar diffusion allows the formation of a relatively massive disc with a size of tens of au in the early disc formation phase, despite a relatively strong magnetic field (e.g. Masson et al. 2016; Zhao et al. 2018; Tsukamoto et al. 2020). By comparing simulations for a coherently rotating core and a turbulent core, Santos-Lima et al. (2012) suggested that turbulence causes small-scale magnetic reconnection and provides an effective mechanism for magnetic diffusion that can remove magnetic flux out of the disc progenitor at time-scales comparable to the collapse, allowing the formation of discs with sizes ~ 100 au. Mignon-Risse et al. (2021) further suggest that, under moderate magnetic fields, massive protostellar discs with radius $\gtrsim 100$ au can only be reproduced in the presence of ambipolar diffusion, even in a turbulent medium. Similar results are reported by Kölligan & Kuiper (2018), Commerçon et al. (2022), and Mignon-Risse et al. (2023), some reporting discs with radius even $\gtrsim 500$ au. Contrastingly, our study shows that in a turbulent environment, where magnetic fields are turbulent and incoherent, large discs can form even without non-ideal MHD effects.

Additionally, the role of cosmic-ray complicates this scenario, as high rates of ionization, shown by Kuffmeier et al. (2020) and Zhao et al. (2016), can suppress the formation of discs. Wurster & Bate (2019) suggest that non-ideal MHD effects moderate the magnetic field in the circumstellar environment, leading to a more constrained range of disc field strengths compared to the ideal-MHD case, which facilitates disc formation. After all, future observations aimed at detecting ion-neutral drift in prestellar cores will be essential in quantifying ambipolar diffusion's significance in disc formation processes.

While our simulations operate within the ideal MHD framework and do not encompass non-ideal MHD effects, the insights garnered in this work on the collapse of massive cores within realistic GMCs are novel, and it is a step towards understanding the interplay between non-ideal MHD phenomena and the role of incoherent, diffused magnetic field lines in the star formation processes. This omission, due to the scope of our investigation, does not diminish the relevance of our findings, but rather it sets the stage for future studies to delve into the comparative impacts of non-ideal versus ideal MHD processes.

5 SUMMARY

We have studied the collapse of strongly magnetized prestellar cores from a set of zoom-in radiation-MHD simulations of star formation in GMCs. The study includes a suite of six simulations of prestellar cores in molecular clouds with varying magnetization ($\mu_0 = 3, 1, 0.6$) and turbulence ($\mathcal{M} = 15, 7$). We come to the following main conclusions:

(1) We find a universal B–ρ relationship, $B \approx 86\ \mu\mathrm{G}\ (n/10^5\ \mathrm{cm}^{-3})^{\frac{1}{2}}$, implying a constant Alfven velocity $v_A \approx 0.5\,\mathrm{km\,s}^{-1}$, for number density in the range between 10^5 and $10^9\ \mathrm{cm}^{-3}$ in the evolution of magnetically critical or super-critical GMCs, regardless of the initial magnetic intensity or cloud size (see Fig. 6). This value of v_A roughly equals the virial velocity of a core with a mass at the peak of the core mass function.

(2) On the large scales of collapsed cores ($r > 10^4$ au), the scaling of the magnetic field with gas density (looking at it on a simulation cell-by-cell basis) is close to $B \propto n^{1/2}$. This is found at densities between 10^5 and $10^9\ \mathrm{cm}^{-3}$ across all GMCs, irrespective of whether the turbulent energy dominates ($\mathcal{M}_A = 5$) or is comparable to the magnetic energy ($\boldsymbol{\mathcal{M}_A = 1}$).

(3) Keplerian circumstellar discs can form in critical and super-critical cores. Subcritical cores, however, fragment into numerous low-mass clumps that undergo direct collapse without any accretion, causing the absence of circumstellar discs (Fig. 2).

(4) Large discs can form in magnetically (near-)critical cores because the magnetic field is extremely turbulent and incoherent, which reduces the effect of magnetic braking by roughly one order of magnitude (see Fig. 10) compared to the scenario where the magnetic field is coherent and perfectly aligned with the rotational axis of the core. The turbulent magnetic field is caused by the supersonic turbulent motion of the gas in the disc, which is plausibly a result of non-axisymmetric accretion of gas enhanced by gravitational collapse.

(5) The cores at the initial phase are near critical with μ ranging between 0.6 and 2 (Fig. 8). These cores are initially predominantly supported by magnetic pressure, with thermal and turbulent pressures playing lesser roles. The discs that form in the cores are supported by both turbulent and magnetic pressure, with the former slightly dominating in the inner part ($\lesssim 1000$ au) and the latter slightly dominating in the outer part. This result, which is contrary to what is typically found in the literature for smaller mass discs, was also found in Paper I and is due to the large masses of the cores studied in this work (30–300 $\mathrm{M}_{\odot}$) and in part to the realistic boundary conditions that generate a continuous source of turbulence through asymmetric inflow. In all our massive discs, thermal pressure support is negligible.

Despite the success of our model in reproducing some key features of circumstellar disc formation, we acknowledge that our study has known limitations. For instance, we do not account for the effects of protostellar outflow/jet feedback, radiation pressure, and radiative heating by low-energy photons on disc evolution. Feedback mechanisms could significantly alter the disc structure and dynamics. And finally, perhaps the most dramatic limitation at these small scales is the ideal-MHD approximation. In future work, we plan to incorporate more realistic stellar feedback prescriptions in our code and possibly non ideal-MHD effects to overcome these limitations and improve the accuracy of our circumstellar disc models.

ACKNOWLEDGEMENTS

CCH acknowledges the support by the National Aeronautics and Space Administration (NASA) FINESST grant 80NSSC21K1850. The authors acknowledge the support of the NASA grant 80NSSC18K0527. The authors also acknowledge the University of Maryland supercomputing resources (http://hpcc.umd.edu) made available for conducting the research reported in this paper.

DATA AVAILABILITY

The data underlying this article were accessed from the University of Maryland supercomputing resources (http://hpcc.umd.edu). The derived data generated in this research will be shared upon reasonable request to the corresponding authors. The software used to do the analysis in this paper is RAMTOOLS, a toolkit to post-process RAMSES-RT simulations and is based on the YT toolkit (https://yt-project.org/doc/index.html), available to download from https://chongchonghe.github.io/ramtools-pages/.

REFERENCES

Allen A., Li Z.-Y., Shu F. H., 2003, ApJ, 599, 363
Bleuler A., Teyssier R., 2014, MNRAS, 445, 4015
Bourke T. L., Myers P. C., Robinson G., Hyland A. R., 2001, ApJ, 554, 916
Codella C. et al., 2014, A&A, 568, L5
Commerçon B., González M., Mignon-Risse R., Hennebelle P., Vaytet N., 2022, A&A, 658, A52
Crutcher R. M., 1999, ApJ, 520, 706
Crutcher R. M., Wandelt B., Heiles C., Falgarone E., Troland T. H., 2010, ApJ, 725, 466
Fielding D. B., McKee C. F., Socrates A., Cunningham A. J., Klein R. I., 2015, MNRAS, 450, 3306
Fromang S., Hennebelle P., Teyssier R., 2006, A&A, 457, 371
Galli D., Lizano S., Shu F. H., Allen A., 2006, ApJ, 647, 374
Galli D., Shu F. H., 1993, ApJ, 417, 243
Geen S., Soler J. D., Hennebelle P., 2017, MNRAS, 471, 4844
Gray W. J., McKee C. F., Klein R. I., 2018, MNRAS, 473, 2124
He C.-C., Ricotti M., 2023, MNRAS 522 5374
He C.-C., Ricotti M., Geen S., 2019, MNRAS, 489, 1880
Hennebelle P., Ciardi A., 2009, A&A, 506, L29
Hennebelle P., Fromang S., 2008, A&A, 477, 9
Hirano S., Tsukamoto Y., Basu S., Machida M. N., 2020, ApJ, 898, 118
Johnston K. G. et al., 2020, A&A, 634, L11
Joos M., Hennebelle P., Ciardi A., 2012, A&A, 543, A128
Joos M., Hennebelle P., Ciardi A., Fromang S., 2013, A&A, 554, A17
Kölligan A., Kuiper R., 2018, A&A, 620, A182
Kuffmeier M., Zhao B., Caselli P., 2020, A&A, 639, A86
Lam K. H., Li Z.-Y., Chen C.-Y., Tomida K., Zhao B., 2019, MNRAS, 489, 5326
Lee C.-F., Li Z.-Y., Ho P. T. P., Hirano N., Zhang Q., Shang H., 2017, Sci. Adv., 3, e1602935
Lewis B. T., Bate M. R., 2018, MNRAS, 477, 4241
Li H.-b., Fang M., Henning T., Kainulainen J., 2013a, MNRAS, 436, 3707
Li Z. Y., Banerjee R., Pudritz R. E., Jørgensen J. K., Shang H., Krasnopolsky R., Maury A., 2014, in Beuther H., Klessen R. S., Dullemond C. P., Henning T., eds, Protostars and Planets VI. University of Arizona Press, Tucson, p. 173
Li Z.-Y., Krasnopolsky R., Shang H., 2013b, ApJ, 774, 82
Machida M. N., Inutsuka S.-I., Matsumoto T., 2011, PASJ, 63, 555
Masson J., Chabrier G., Hennebelle P., Vaytet N., Commerçon B., 2016, A&A, 587, A32
Mellon R. R., Li Z.-Y., 2008, ApJ, 681, 1356
Mestel L., Spitzer L., 1956, MNRAS, 116, 503
Mignon-Risse R., González M., Commerçon B., Rosdahl J., 2021, A&A, 652, A69
Mignon-Risse R., Oliva A., González M., Kuiper R., Commerçon B., 2023, A&A, 672, A88
Mocz P., Burkhart B., Hernquist L., McKee C. F., Springel V., 2017, ApJ, 838, 40
Murillo N. M., Lai S.-P., Bruderer S., Harsono D., van Dishoeck E. F., 2013, A&A, 560, A103

O'dell C. R., Wen Z., 1992, ApJ, 387, 229
Rees M. J., 1976, MNRAS, 176, 483
Rosdahl J., Blaizot J., Aubert D., Stranex T., Teyssier R., 2013, MNRAS, 436, 2188
Santos-Lima R., de Gouveia Dal Pino E. M., Lazarian A., 2012, ApJ, 747, 21
Seifried D., Banerjee R., Pudritz R. E., Klessen R. S., 2013, MNRAS, 432, 3320
Teyssier R., 2002, A&A, 385, 337
Teyssier R., Commerçon B., 2019, Front. Astron. Space Sci., 6 51
Tobin J. J., Hartmann L., Chiang H.-F., Wilner D. J., Looney L. W., Loinard L., Calvet N., D'Alessio P., 2012, Nature, 492, 83
Troland T. H., Heiles C., 1986, ApJ, 301, 339
Tsukamoto Y., Okuzumi S., Iwasaki K., Machida M. N., Inutsuka S., 2018, ApJ, 868, 22
Tsukamoto Y., Machida M. N., Susa H., Nomura H., Inutsuka S., 2020, ApJ, 896, 158
Tsukamoto Y. et al., 2023, in Inutsuka S., Aikawa Y., Muto T., Tomida K., Tamura M., eds, ASP Conf. Ser. Vol. 534, Protostars and Planets VII. Astroc. Soc. Pac., San Francisco, p. 317
Wurster J., Bate M. R., 2019, MNRAS, 486, 2587
Wurster J., Lewis B. T., 2020, MNRAS, 495, 3795
Wurster J., Price D. J., Bate M. R., 2016, MNRAS, 457, 1037
Yen H. W., et al. 2023, ApJ, 942, 32
Zapata L. A., Ho P. T. P., Rodríguez L. F., Schilke P., Kurtz S., 2007, A&A, 471, L59
Zhao B., Li Z.-Y., Nakamura F., Krasnopolsky R., Shang H., 2011, ApJ, 742, 10
Zhao B., Caselli P., Li Z.-Y., Krasnopolsky R., Shang H., Nakamura F., 2016, MNRAS, 460, 2050
Zhao B., Caselli P., Li Z.-Y., Krasnopolsky R., 2018, MNRAS, 473, 4868

APPENDIX A: MASS-TO-FLUX RATIO OF A NON-SINGULAR ISOTHERMAL SPHERE

The density profile of a non-singular isothermal core in hydrostatic equilibrium is given by

$$\rho(r) = \frac{\rho_0}{1+(\frac{r}{r_c})^2}. \tag{A1}$$

Defining the dimensionless radius $\xi \equiv r/r_c$, we can show that the mass of the gas within ξ is $M(\xi) = 4\pi\rho_0 r_c^3(\xi - \arctan\xi)$. Assuming a parallel magnetic field threading the mid-plane of the sphere with the magnetic strength proportional to $\rho^{1/2}$ and equal to B_0 a the centre, then we have

$$\Phi_B = \int_0^{\xi_1} 2\pi r_c \xi \frac{B_0}{\sqrt{1+\xi^2}} r_c d\xi = 2\pi B_0 r_c^2\left(\sqrt{1+\xi_1^2}-1\right). \tag{A2}$$

The magnetic critical mass is given by equation (2).

The gravitational binding energy of a core with radius ξ_1 is given by this integral

$$\begin{aligned} W &= -\int_0^{\xi_1} GM(\xi)4\pi r\rho(r)r_c \mathrm{d}\xi \\ &= -(4\pi)^2 G\rho_0^2 r_c^5 \int_0^{\xi_1} \frac{\xi(\xi-\arctan\xi)}{1+\xi^2}\mathrm{d}\xi. \end{aligned} \tag{A3}$$

The total magnetic energy inside radius ξ_1 is

$$\begin{aligned} e_B &= \int_0^{\xi_1} 2\pi r_c^2 \xi \mathrm{d}\xi 2r_c\sqrt{\xi_1^2-\xi^2}\frac{1}{8\pi}\frac{B_0^2}{1+\xi^2} \\ &= \frac{1}{2}B_0^2 r_c^3\int_0^{\xi_1}\frac{\xi\sqrt{\xi_1^2+\xi^2}}{1+\xi^2}\mathrm{d}\xi. \end{aligned} \tag{A4}$$

We plot $\mu_1 = M/M_\Phi$ and $\mu_2 = \sqrt{|W|/e_B}$ for an isothermal core with $\rho_0 = 10^9 m_p$ cm^{-3}, $r_c = 1000$ au, and $B_0 = 0.01$ Gauss in the top panel of Fig. A1. In the bottom panel, we show the value of the equivalent geometrical factor $c_\Phi = \sqrt{G}M/(\Phi_B\mu_2)$ in equation (2), required to have $\mu_2 = \mu_1$.

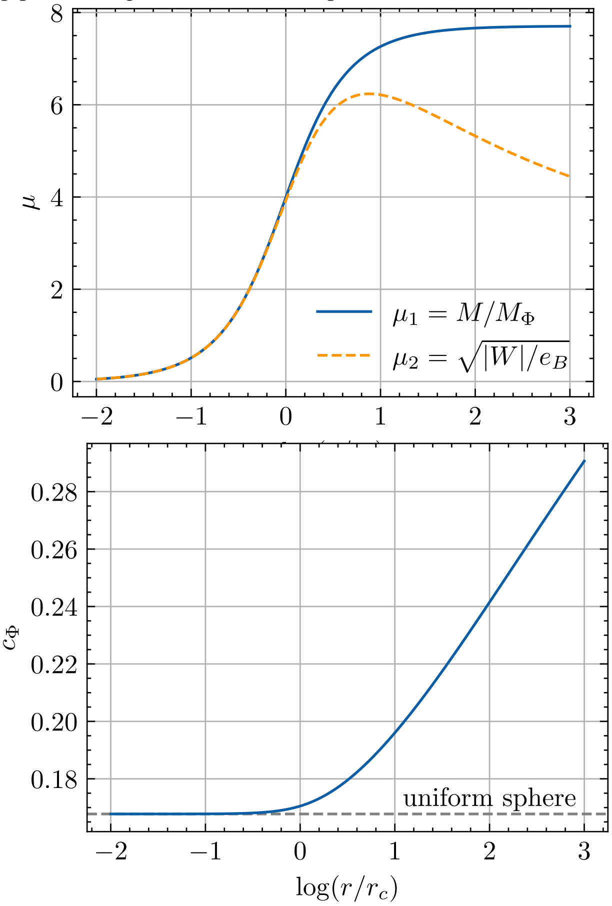

Figure A1. Comparing two definitions of the relative importance of the gravitational and magnetic forces in a non-singular isothermal sphere as a function of its radius: the relative mass-to-flux ratio $\mu_1 = M/M_\Phi$ and the square root of the binding to magnetic energy $\mu_2 = \sqrt{|W|/e_B}$. In the former case, the geometrical factor c_Φ in equation (2) equals $1/\sqrt{2}$. The value of c_Φ required for the two definitions of μ to be equivalent to each other (i.e. $\mu_1 = \mu_2$) is shown in the bottom panel, showing that c_Φ increases as the core becomes more centrally concentrated.

This paper has been typeset from a TEX/LATEX file prepared by the author.